Collective magnetization dynamics in nanoarrays of thin FePd disks

Agne Ciuciulkaite,[1,*] Erik Östman,[1] Rimantas Brucas,[2,3] Ankit Kumar,[2] Marc A. Verschuuren,[4] Peter Svedlindh,[2] Björgvin Hjörvarsson,[1] and Vassilios Kapaklis[1,†]

[1]*Department of Physics and Astronomy, Uppsala University, Box 516, SE-75120 Uppsala, Sweden*
[2]*Department of Engineering Sciences, Uppsala University, Box 534, SE-751 21 Uppsala, Sweden*
[3]*Ångström Microstructure Laboratory, Uppsala University, Box 534, SE-751 21 Uppsala, Sweden*
[4]*Philips Research Laboratories, High Tech Campus 4, Eindhoven, The Netherlands*

(Received 5 February 2019; revised manuscript received 10 April 2019; published 14 May 2019)

We report on the magnetization dynamics of a square array of mesoscopic disks, fabricated from an iron palladium alloy film. The dynamics properties were explored using ferromagnetic resonance measurements and micromagnetic simulations. The obtained spectra exhibit features resulting from the interactions between the disks, with a clear dependence on both temperature and the direction of the externally applied field. We demonstrate a qualitative agreement between the measured and calculated spectra. Furthermore, we calculated the mode profiles of the standing spin waves excited during time-dependent magnetic field excitations. The resulting maps confirm that the features appearing in the ferromagnetic resonance absorption spectra originate from the temperature- and directional-dependent interdisk interactions.

DOI: 10.1103/PhysRevB.99.184415

I. INTRODUCTION

Arrays of closely packed mesoscopic magnets provide a rich playground for investigations of collective magnetization dynamics. The (stray field induced) interaction between the disks forms a link between the internal magnetization dynamics of the elements and the global response of the system[1–4]. Magnetic disks are interesting in this context due to the richness of internal magnetic textures and the absence of shape induced anisotropy in their plane. Disks of certain radius and height ratio exhibit a ground state referred to as a *vortex* [5,6] characterized by an in-plane magnetic flux closure. Since the magnetic moments are curling in-plane of the disks, the stray field from the disks is negligible when vortices are formed, in stark contrast to the *collinear state* [7–10]. The application of an external magnetic field drives the vortex core out of the center, towards the edge of the disk. At a given field, the vortex is annihilated and the magnetic moment is aligned parallel to the direction of the applied field (collinear state). When the disks are in a collinear state, their stray fields result in interdisk interactions. Previous investigations of iron-palladium ($Fe_{20}Pd_{80}$) disks, arranged in a square array (see Fig. 1), showed that a change of temperature is sufficient to alter the magnetization dynamics [10]. Above a given temperature the energy barrier for switching from a vortex to the collinear state and vice versa was even found to be free from hysteresis. As a consequence, the magnetization state of the system under a certain applied field becomes bistable: the vortex and the collinear state have the same energy. Ferromagnetic resonance (FMR) is a suitable technique for investigation of magnetization dynamics of ferromagnetic films and structures in different magnetization states [18]. FMR resonance dependence on the direction of external magnetic field and spacing between magnetic mesoscpic elements has been previously reported for various patterned nanostructures, such as nickel and permalloy nanowire arrays [12], permalloy rectangles [13], and antidot [14–16] arrays.

Here we explore the effect of changes in the interdisk interactions on the magnetization dynamics of soft magnetic iron-palladium alloy disks, using FMR and micromagnetic simulations [11]. The changes in the interdisk interactions are obtained by rotating the magnetization of the disks as well as altering the stray field from the disks by changing the sample temperature. Computing spatial profiles of standing spin wave modes [14–16], we investigate their dependence on the modification of the interaction and compare to the experimental resonance spectra.

II. METHODS

A. Sample

The sample was fabricated by magnetron co-sputtering of elemental Fe and Pd targets, using Ar as sputtering gas (base pressure $<10^{-7}$ Pa) on a prepatterned fused silica substrate. The substrate was prepatterned by surface conformal nanoimprint lithography. As a result, the investigated array consists of iron-palladium alloy ($Fe_{20}Pd_{80}$) disks arranged in a square lattice as illustrated in Fig. 1. Each disk has a radius of 225 nm and a thickness of 10 nm, with a center-to-center distance of the disks equal to 513 nm in the [10] direction. This results in an interdisk distance of 53 and 275 nm along the [10] and along the [11] direction, respectively. A more detailed description of the sample preparation is provided by Östman *et al.* [10].

*agne.ciuciulkaite@physics.uu.se
†vassilios.kapaklis@physics.uu.se

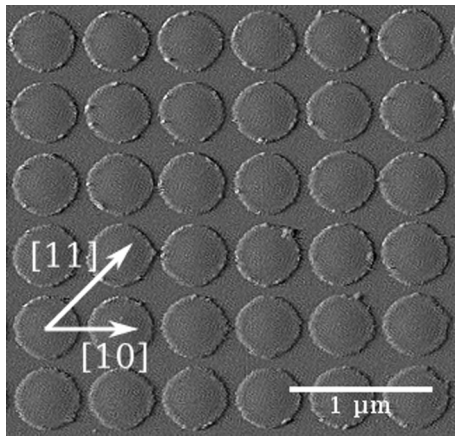

FIG. 1. Atomic force microscopy image of a square array of $Fe_{20}Pd_{80}$ alloy disks with the high symmetry directions indicated as [10] and [11] by arrows.

B. Ferromagnetic resonance measurements

Magnetization dynamics of the $Fe_{20}Pd_{80}$ disk arrays were measured using X-band cavity FMR equipped with a variable-temperature sample holder. A static magnetic field was applied in-plane, while a time-dependent spatially uniform (wave vector $\vec{k} = 0$) magnetic field excitation, with a frequency of 9.8 GHz, was applied perpendicular to the plane of the sample [7,17]. The static magnetic field was swept from 0 to 300 mT and the measurements were carried out at temperatures ranging from 80 to 293 K. The strength of the applied static field ensured that disks were measured in the collinear state.

A second set of FMR measurements were performed using a vector-network analyzer (VNA) at room temperature, by an in-plane field sweep, utilizing a coplanar waveguide. The detailed description of this measurement setup is described by Wei *et al.* [18]. The linewidth ΔH_t versus frequency f data obtained from these measurements were fitted to a linear function, extracting the Gilbert damping coefficient α. The extracted value for α was 1.8×10^{-2} and was later employed as a parameter in the micromagnetic simulations of the magnetization dynamics in the $Fe_{20}Pd_{80}$ disk array. It was adjusted in order to match the calculated FMR absorption peak amplitude to one measured experimentally.

C. Micromagnetic simulations and standing spin wave map calculations

Micromagnetic simulations were performed using MuMax3 [19]. The exchange stiffness constant A_{ex} defining the interspin coupling in the magnetic material was adjusted to qualitatively reproduce the experimental observations. It is known that A_{ex} is temperature dependent and decreases with increasing temperature [20]. Therefore a higher temperature implies softer standing spin wave modes, excited within the disks. The initial simulations were carried out using the saturation magnetization corresponding to 300 K in order to determine which A_{ex} value reproduces the experimentally obtained FMR absorption spectra at the same temperature. A value of $A_{ex} = 3.36$ pJ/m resulted in the micromagnetic simulations reproducing the experimental spectra and was thus chosen for subsequent simulations in order to limit the simulation parameter space. A broader discussion and motivation regarding this choice is provided by Ciuciulkaite [21]. Finally, the Gilbert damping parameter α describing the losses in the system and being proportional to the FMR absorption linewidth was chosen to be 1.9×10^{-2}, after fine tuning of the initial value determined from the VNA-FMR measurements.

In the micromagnetic simulations, four disks with 225 nm radius and 10 nm thickness were placed in a 2-by-2 square lattice with a lattice parameter of 513 nm. The in-plane cell size was defined as $0.513(18)l_{ex}$, where l_{ex} is the exchange length, a material parameter determined by the A_{ex} and M_{sat} [19]. The cell size along the z direction, i.e., the thickness of the structure, was set to 5 nm for all simulations. Periodic boundary conditions (PBC) [19] were applied in both lateral directions ($PBC_x = PBC_y = 3$, $PBC_z = 0$). The FMR simulations were performed by applying a static magnetic field in-plane of the lattice, relaxing the system, and then applying a time-dependent field excitation out-of-plane, with an analytical expression of $A\sin(2\pi ft)$ or $A\,\mathrm{sinc}(2\pi ft)$. The static magnetic field is applied at an angular offset of 2° from the principal in-plane directions in order to lift any degeneracy in the simulations, related to the high symmetry directions we will be investigating, being parallel to the [10] and [11] direction of the disk lattice. The amplitude of the time-dependent excitation was $A = 5$ mT, the frequency was $f = 9.8$ GHz, the duration of the sinusoidal time-dependent magnetic field excitation was 10 ns, and the sampling period was 1 ps. The frequency bandwidth for the sinc function excitation was 20 GHz. The temperature-dependent saturation magnetization $M_{sat}(T)$ was used to account for the temperature dependence of the FMR response of the soft magnetic disks. The $Fe_{20}Pd_{80}$ alloy has a Curie temperature T_C of 463 K [10]. To a first approximation the temperature dependence of the magnetization can be described by the modified Bloch behavior:

$$M_{sat}(T) = M_{sat}(0)\left[1 - \left(\frac{T}{T_C}\right)^{\beta}\right], \tag{1}$$

where $M_{sat}(0)$ is the saturation magnetization at 0 K and is 5.9×10^5 A/m for the $Fe_{20}Pd_{80}$ alloy and $\beta = 1.69$ [10]. Here we would like to note that we do not account for any other temperature induced effects in our simulations than the temperature dependence of the saturation magnetization.

A complementary method for describing the observed features in the FMR spectra are standing spin wave (SSW) mode maps. The maps were calculated from the spatial micromagnetic evolution of the magnetization applying a 9.8 GHz microwave magnetic field. A fast Fourier transform (FFT) for each of the discrete spatial elements was performed, resulting in the spatial maps of the amplitude of the magnetization dynamics.

III. RESULTS AND DISCUSSION

A. FMR

The FMR spectra measured at room temperature, with the static field applied along [10] and [11] in-plane directions

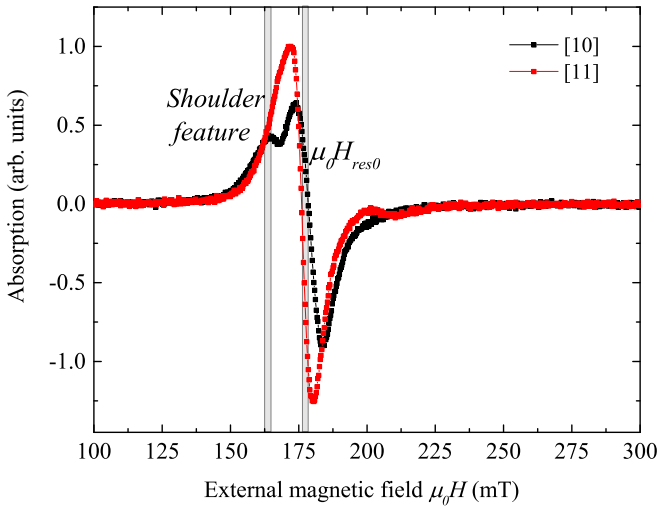

FIG. 2. The measured FMR spectra of square arrays at room temperature with the field applied along [10] and [11] directions. The shaded gray regions indicate characteristic FMR absorption features of the investigated structure: A *shoulder feature*, appearing before the main absorption peak, and a main FMR field, $\mu_0 H_{\mathrm{res0}}$.

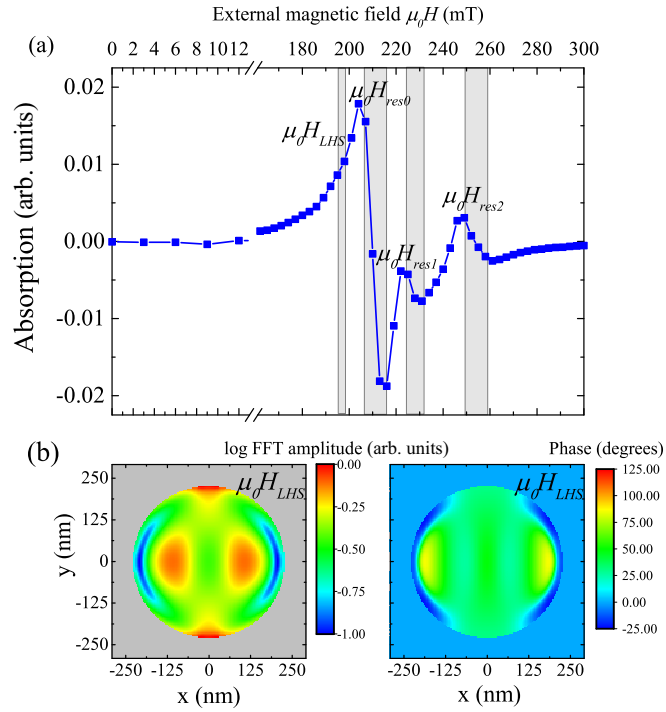

FIG. 3. (a) FMR absorption spectrum for a single disk, taken as a line cut from the map in Fig. 8 (see Appendix A) at 9.8 GHz frequency. The shaded gray regions indicate external magnetic fields at which the SSW profiles (m_z component, amplitude of precession) were calculated. (b) FFT amplitude and phase maps calculated at a shoulder feature at 197(3) mT applied magnetic field.

of the array, as indicated in Fig. 1, are shown in Fig. 2. The ferromagnetic resonance shifts to slightly higher applied magnetic fields when the field is applied along [10] direction as compared to the [11] direction. Shifts in the ferromagnetic resonance fields, upon change of the external magnetic field direction, have also been observed in studies of antidot lattices [14–16]. This shift reflects the effect of the interdisk interaction strength due to the change in the applied static magnetic field and hence the stray field direction. Furthermore, the measured FMR absorption spectra exhibits a split in the main absorption peak in the [10] direction at around 163.0(3) mT. We will call this feature before the main absorption peak a *shoulder feature* (see Fig. 2 in the following). The change in interaction strength is due to a modification of interdisk coupling by changing the magnetization direction of the disks. Effectively, from the magnetic interactions point of view, along the [10] direction a disk has two nearest neighbors while along the [11] direction the number of interacting nearest neighbors is doubled as shown later in Sec. III D.

B. Micromagnetic simulations on a single disk

Micromagnetic simulations of a single disk were carried out to identify the basic features of the elements, i.e., the response of the disks in absence of interactions. A FMR frequency versus an applied static field map was calculated for a wide range of frequencies, using the expression $A\,\mathrm{sinc}(2\pi f t)$ for the time-dependent magnetic field excitation and is provided in Appendix A, Fig. 8. Since the FMR measurements were carried out at the frequency of 9.8 GHz, a line cut along this frequency was taken and is shown as an FMR absorption spectrum in Fig. 3(a). The shaded gray regions indicate the strength of the applied static magnetic field, for which the SSW modes excited in the disk were simulated and are presented as maps of normalized magnetization precession amplitude and phase in Fig. 3(b) and in Appendix B Fig. 9.

Figure 3(b) presents the SSW maps for an amplitude and phase for applied magnetic field corresponding to the region where the shoulder feature in Fig. 2 is observed. It is indicated on the left-hand side (LHS) of the main absorption peak as $\mu_0 H_{\mathrm{LHS}}$ in Fig. 3(a). This mode is mainly constrained near the middle of the disk and along a line parallel to the direction of the applied magnetic field ([10] direction). In the remainder of this paper we will refer to the area in the middle of a disk as the *central* area. The largest precession takes place at two symmetric points outside of the disk center, along the direction of static magnetic field. In addition to these symmetry points, the magnetic moments also resonate at the edges of the disk along a line perpendicular to the magnetic field direction. In the following we will refer to this mode as a *perpendicular edge* mode. To SSW modes appearing at the edges along a line parallel to the direction of the applied magnetic field, we will be referring to as *parallel edge* modes. The SSW spatial mode maps calculated at higher magnetic fields indicate the following spatial mode profiles: at 216(3) mT field—uniform precession, at 232(3) and 256(3) mT—edge modes (see Appendix B Fig. 9).

C. Micromagnetic simulations of square arrays

Subsequent simulations were carried out on square arrays containing interacting disks, but otherwise identical to the building block described in the previous section. In order to explain the shoulder feature in the FMR spectra for the [10] direction (Fig. 2) and to further investigate which SSW modes

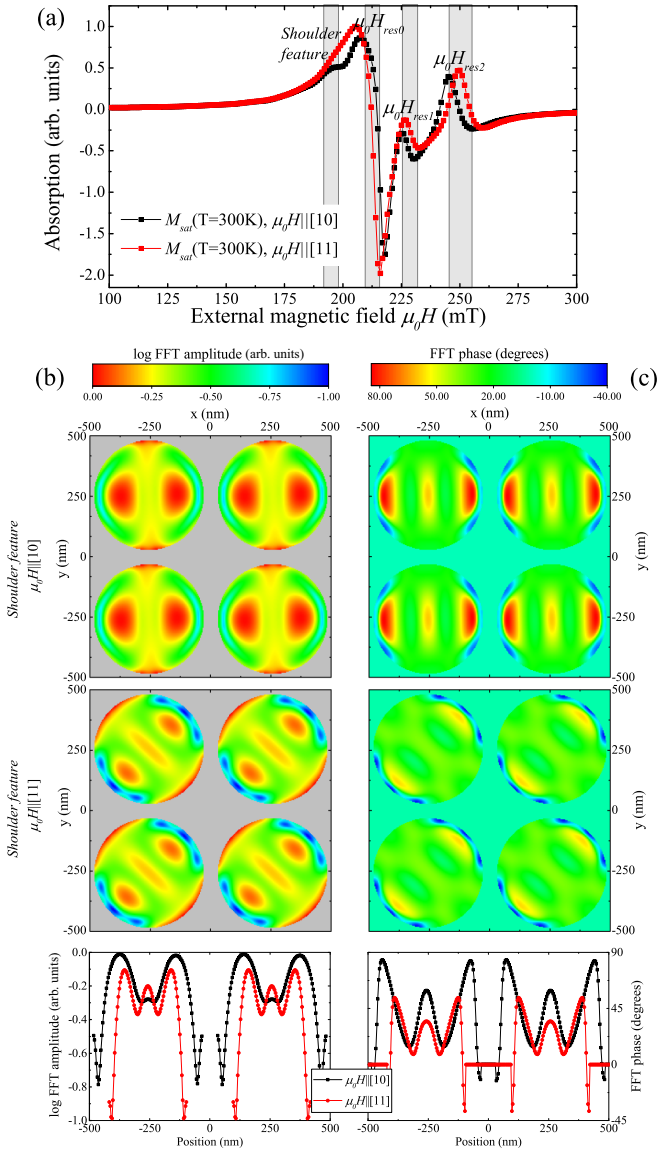

FIG. 4. (a) Computed FMR absorption spectra with $M_{\rm sat}(T = 300$ K) and static magnetic field applied along the [10] and [11] directions. Gray shaded regions represent external magnetic fields indicated as shoulder features, $\mu_0 H_{\rm res0}$, $\mu_0 H_{\rm res1}$, and $\mu_0 H_{\rm res2}$, at which SSW modes were calculated (correspondingly, for [10] direction: 186, 216, 229, and 251 mT, while for [11] direction: 191, 214, 230, and 255 mT). (b) Spatial amplitude and (c) phase maps of SSW modes calculated for the two applied field directions. Color bars indicate normalized amplitude and phase angles in degrees; the bottom panels in (b) and (c) represent amplitude and phase line cuts in the respective maps along the [10] and [11] directions.

are excited in the disks, spatial amplitude and phase maps [see Figs. 4(b) and 4(c)] were calculated at external magnetic fields of 191 and 186 mT along the [10] and [11] directions, respectively.

The shoulder feature on the left-hand side of the FMR absorption peak, observed in the experimentally measured spectra (Fig. 2), is also present in the calculated results, when the external magnetic field is applied along the [10] direction [Fig. 4(a)]. In this case, calculated SSW mode spatial maps show that the magnetic moments are strongly out of phase at the *parallel edge* and *center* areas of the disks. When the direction is changed to [11], the interaction strength between the disks is modified, due to effective increase of nearest neighbors along the [11] direction and the magnetic moment precession amplitude significantly increases in the center and perpendicular edge areas. Simultaneously, the phase angles in the center and at the parallel edges of a disk decrease, while the overall phase angle distribution over each disk becomes more uniform as compared to the case when the external field is along the [10] direction. Furthermore, the amplitude of the perpendicular edge mode and the extension over the edges is smaller for the [10] external field direction as compared to the [11] direction. This again is a hallmark of the effect the proximity to the nearest neighboring disks has on the magnetization dynamics. Comparison of the SSW mode amplitude and phase spatial maps, to those of an isolated single disk, reveals that the amplitude of magnetic moments in the center of an isolated disk is smaller as compared to the same area in the arrays.

These results clearly demonstrate the effect of the stray field coupling between disks in an array on the internal magnetization dynamics of the elements. Modifying the interdisk interaction strength alters the magnetic moment fluctuations at the center of a disk which results in appearance (or disappearance) of the shoulder feature in an FMR absorption spectrum. A further important observation arising from the simulations is the absorption modes appearing at higher fields after the main absorption peak. These features, indicated as $\mu_0 H_{\rm res1}$ and $\mu_0 H_{\rm res2}$ at around 229(3) and 251(3) mT, respectively, in Fig. 4(a), are not observed in the experimental FMR spectra (Fig. 2). These modes can be identified as edge modes [14–16,22]. They arise from the idealized circular shape of the disks in the simulations and are sensitive to the direction of an external magnetic field in a similar way as the edge localized modes investigated in an antidot lattice by Sklenar *et al.* [14]. In real samples the lithographically fabricated elements are imperfect, leading to the absence of these modes [22]. The origin of spin wave profiles for these simulated modes is discussed in more detail in Appendix C.

D. Ferromagnetic resonance response of iron-palladium arrays: Comparison of experiments and simulations

A comparison of the measured and calculated spectra is provided in Fig. 5, where we display the change in the ferromagnetic resonance field [indicated as $\mu_0 H_{\rm res0}$ in Figs. 2 and 4(a)] with increasing temperature, for applied fields in the [10] and [11] directions. The strength of the interaction alters the resonance field as observed in the measured FMR spectra. The same qualitative changes are observed in the micromagnetic simulations. The resonance field increases as the temperature is increased (see Fig. 5). Thermal fluctuations become more prominent with increasing temperature and a stronger magnetic field is needed to align the moments, shifting the resonance field to higher values. This trend is seen in both calculated and measured FMR spectra. At low temperatures the experimental and calculated resonance fields are comparable. At elevated temperatures the resonance fields calculated from micromagnetic simulations increase faster

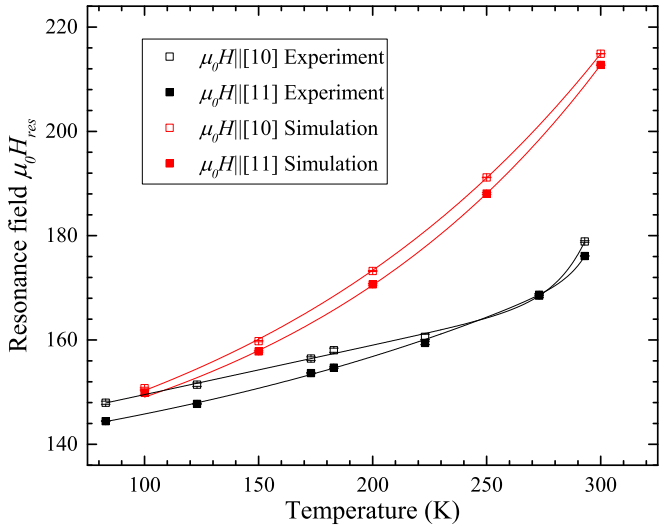

FIG. 5. Comparison of the resonance fields obtained via micromagnetic simulations (red squares) and experimental values (black squares) extracted from FMR measurements of the $Fe_{20}Pd_{80}$ alloy disk array. The external static magnetic field was applied along [10] and [11] directions (empty and filled symbols, respectively). Lines are guides to the eye. Error bars and resonance fields were obtained from fitting of FMR amplitude to a Lorentzian peak profile.

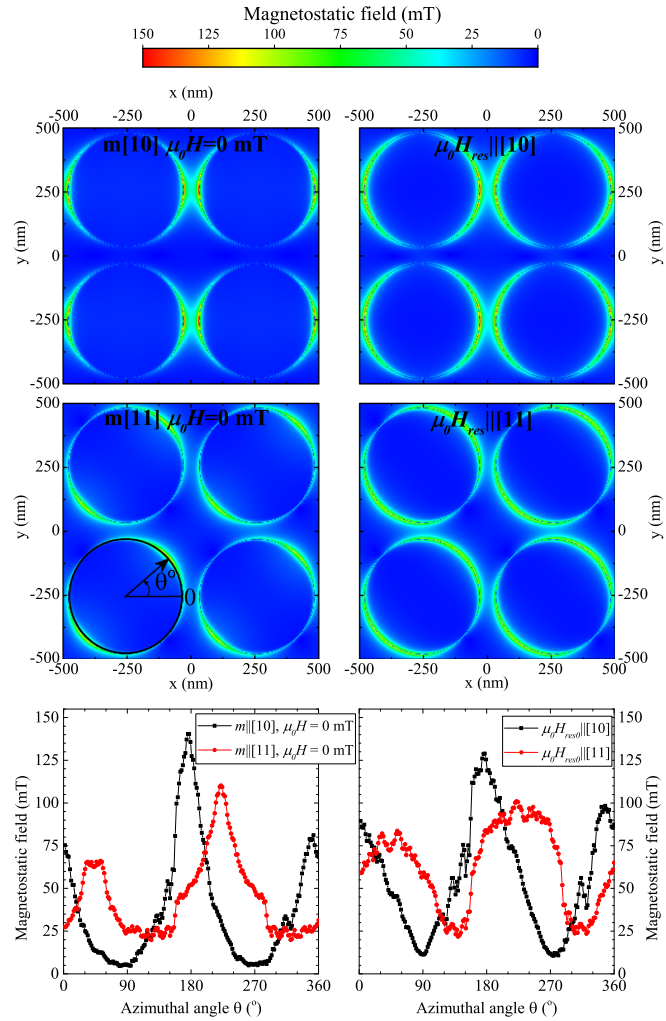

FIG. 6. Spatial distribution maps of demagnetizing field strengths, obtained from micromagnetic simulations of arrays with initial magnetization along [10] and [11] directions (first and second row, respectively) relaxed in a 0 mT static magnetic field and a field corresponding to the ferromagnetic resonance field (left and right columns, respectively). Bottom panels represent polar plots of the demagnetizing field, along the rim of a disk, as indicated by a circle in the "m[11]$\mu_0 H = 0$ mT" map.

than the measured values. The micromagnetic simulations offer a qualitative agreement with the experimental data which is more clearly seen from a comparison of measured (Fig. 2) and calculated FMR absorption spectra [Fig. 4(a)] at elevated temperatures.

In Fig. 5 we can further observe that the splitting between the simulated resonance field values along [10] and [11] directions is always present in the investigated temperature range. The curves for the [10] direction lie higher in field, compared to those for the [11] direction in the investigated temperature range. In related studies, where neighboring elongated micromagnetic elements were antiferromagnetically coupled by stray fields, resonance field shifts depending on the strength of the interaction were also reported [12,13]. However, the difference in resonance field for [10] and [11] directions ($H_{\mathrm{res}[10]} - H_{\mathrm{res}[11]}$) calculated from micromagnetic FMR results (by fitting amplitude to a Lorentzian profile peak and extracting its position), follows a different trend as compared to the resonance field extracted from experimentally obtained data (Fig. 5). This can be attributed to the fact that while exchange stiffness and Gilbert damping parameters are temperature dependent, in micromagnetic simulations we kept these parameters constant for all temperatures. Furthermore, no thermal fluctuations were accounted for in micromagnetic simulations.

Finally, we would like to comment upon the scaling of the experimental resonance field difference $H_{\mathrm{res}[10]} - H_{\mathrm{res}[11]}$ versus temperature. The difference decreases monotonically up to some temperature, where it effectively becomes zero, while beyond that it seems to increase again. This behavior potentially relates to the internal magnetization dynamics within the disks. As already reported previously for the same sample, by Östman *et al.* [10], a temperature range exists where bistability is attainable for the collinear and vortex states, which should also be accompanied by a strong modification in the magnetization dynamics of the individual disks. This range was found to be independent of applied field direction, for temperatures above ≈220 K from measurement protocols involving very low frequencies (hysteresis curves, recorded employing the magneto-optical Kerr effect and field cycling of 0.4 Hz). In the present study, $H_{\mathrm{res}[10]} - H_{\mathrm{res}[11]}$ becomes zero at ≈270 K, considerably higher than that in Östman *et al.* [10]. The timescale of dynamics, probed in this work, is much shorter (sub-nanoseconds, FMR measured at 9.8 GHz), hinting for this strong apparent temperature shift.

The shift in the resonance field is attributed to a difference in the stray field induced inter-disk coupling, along the [10] and [11] directions. In Fig. 6 we show the spatial maps of the demagnetizing field amplitude, computed for arrays with

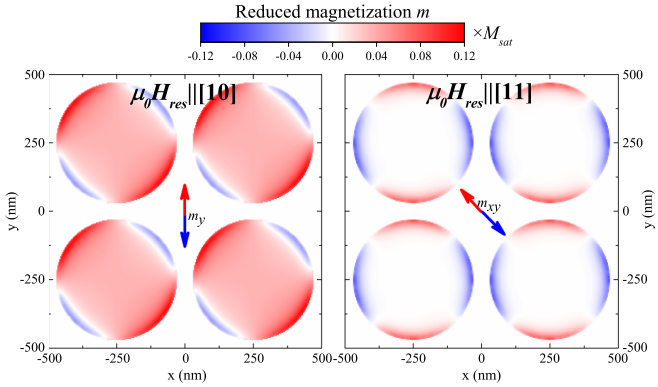

FIG. 7. Spatial maps of magnetization components distribution perpendicular to the direction of the external magnetic field. Maps were obtained from micromagnetic simulations of arrays with initial magnetization along [10] and [11] directions relaxed in a static magnetic field corresponding to H_{res} in magnitude for each of the directions.

initial collinear magnetization states, along [10] and [11] directions. Having the magnetization of the elements along the [11] direction results in an increased stray field coupling between neighboring disks. Even though the spacing between neighboring disks in the [10] direction is smaller—and thus one would expect a stronger coupling—the demagnetizing field strength is distributed broadly along the disk perimeter for the [11] case (see the bottom panels in Fig. 6). This leads to a stronger coupling for the applied fields along the [11] direction. The root of these effects are clearly seen in Fig. 7, where we provide spatial maps of static magnetization components perpendicular to the direction of applied magnetic field. Both of the maps reveal a so called "onion" state for the magnetization.

A map of the m_y component with $H_{\text{res}}||$ [10] shows a dominant positive direction for these, in accordance to the 2° offset of H_{res} from the [10] direction in our simulations. When $H_{\text{res}}||$ [11], the magnetization components m_{xy} perpendicular to applied fields, obtain nonzero values only at the disks' rim and with maxima at the positions where the gap to neighboring disk is minimum. In contrast to the case where $H_{\text{res}}||$[10], now all of the four gaps related to neighboring disks are active. The maps show that $m_{xy} \perp$ [11] is of the same sign at the disk edges along the [10] and [01] directions which further confirm interdisk coupling via stray fields. A similar effect was observed by Martyanov *et al.* [16], where the inner magnetic structure was shown to be strongly dependent on the direction of the external magnetic field.

IV. CONCLUSIONS

We have investigated the magnetization dynamics in a square array of $Fe_{20}Pd_{80}$ alloy disks by means of FMR measurements and micromagnetic simulations. The ferromagnetic resonance is found to increase in field with increasing temperature which we attribute to the decrease of the magnetic moment. The results were qualitatively reproduced and confirmed by micromagnetic simulations. The effects of stray field induced interaction of the islands are seen in the orientation dependence of the resonance field as well as the fine structures of the resonance. The interisland interaction is found to be larger when the magnetization of the islands are in the [11] as compared to [10] principal directions. The origin of this effect arises from the transverse component of the magnetization, enhancing the interisland interactions in the transverse directions. This illustrates the importance of the interisland interactions in modifying and affecting the inner magnetic structure [14–16] of a thin mesoscopic magnetic element. Accounting for this, we analyze and explain results of both the static and dynamic magnetization response of arrays containing magnetically soft $Fe_{20}Pd_{80}$ alloy disks. These concepts can be utilized for analyzing and designing the microwave response of extended arrays of thermally active and interacting nanomagnets [23–25], having interesting topological and interaction schemes, such as artificial spin ices [1,3,4,26–29]. The latter could enable the design and fabrication of reconfigurable magnonic devices [3,27].

ACKNOWLEDGMENTS

The authors would like to acknowledge financial support from the Swedish Research Council (VR), the Swedish Foundation for International Cooperation in Research and Higher Education (STINT), and the Knut and Alice Wallenberg Foundation project "*Harnessing light and spins through plasmons at the nanoscale*" (2015.0060). This work is part of a project which has received funding from the European Union's Horizon 2020 research and innovation programme under Grant agreement No. 737093. V.K. would like to thank Prof. P. Poulopoulos, University of Patras, Greece, for fruitful discussions.

APPENDIX A: DISPERSION RELATION OF A SINGLE FePd DISK

The complete map of available resonance modes for a single nanodisk resonator is shown in Fig. 8 as a frequency vs external magnetic field map. The color bar represents the log FFT amplitude of spin precession. Below the annihilation

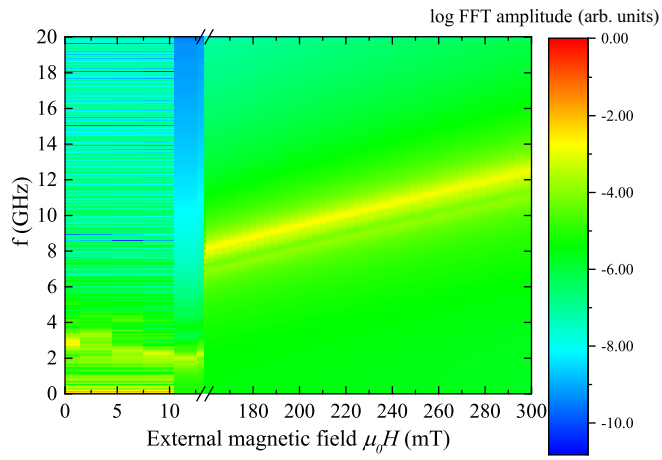

FIG. 8. The calculated map of the log and normalized FMR amplitude response to a 20 GHz bandwidth sinc function form magnetic field excitation, for different external static fields.

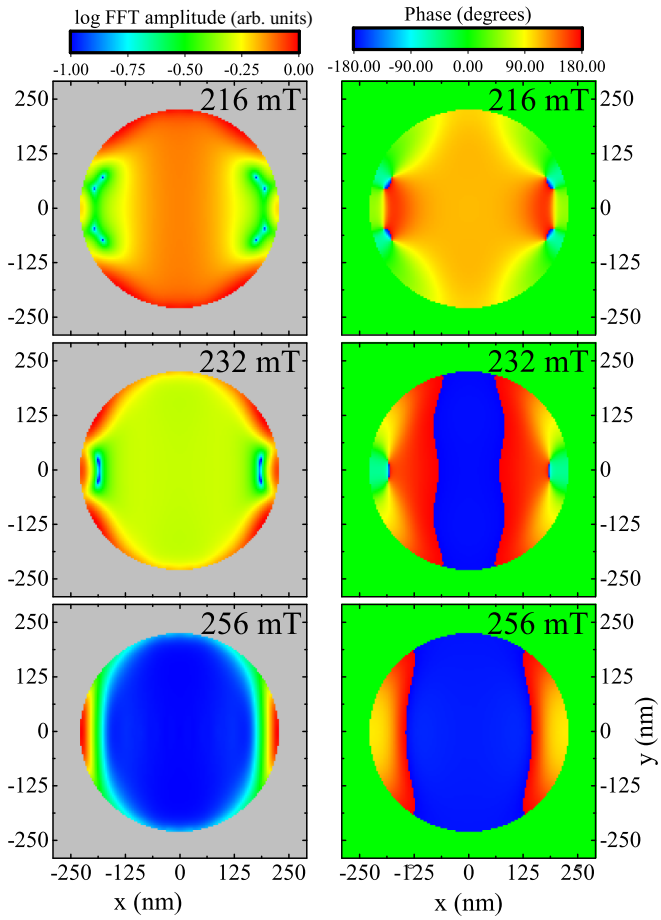

FIG. 9. The calculated spatial log and normalized FFT amplitude and phase maps of an isolated single disk at different fields indicated in Fig. 3(a).

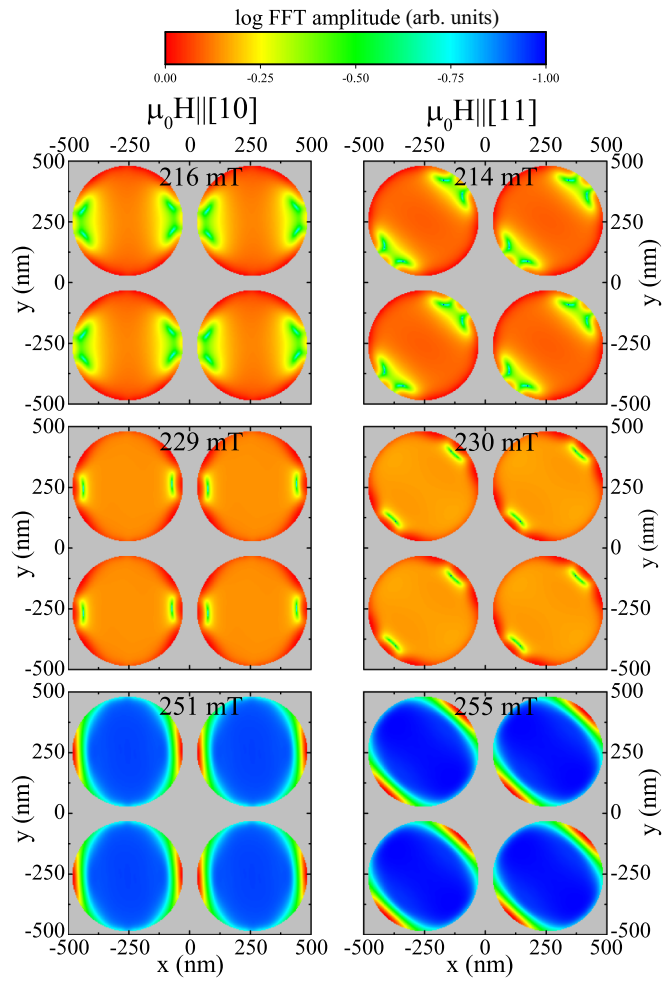

FIG. 10. Spatial maps of SSW modes calculated for the $Fe_{20}Pd_{80}$ alloy disk array at the field values indicated by shaded gray regions in Fig. 4(a).

field, the spectrum is dominated by low frequency modes, corresponding mostly to the gyrotropic motion of the vortex core [30]. The highest intensity peak corresponding to a vortex mode shows similar dispersion relation as that for isolated cylinders exhibiting single domain state [12]. At stronger external magnetic fields above the saturation field, when the disk is in a collinear magnetic state, a significant increase of the resonance frequency is observed and highest intensity peak follows Kittel-like behavior of resonance frequency for continuous ferromagnetic films. Below the main resonance peak are two smaller intensity features following a Kittel-like behavior, corresponding to the edge modes.

APPENDIX B: MAGNETIZATION MAPS OF SINGLE DISK SSW MODES

SSW maps calculated at the resonance field, which is 210 mT for a single disk, reveal that the area of constrained magnetic moments becomes more concentrated at the edges along the direction of an applied magnetic field. Meanwhile, magnetic moment fluctuations become more intense at the *perpendicular edges*. In contrast, the SSW modes calculated at 226 and 255 mT external magnetic fields appear at the *parallel edges*. The spatial log normalized FFT amplitude and phase maps calculated at fields just below the ferromagnetic resonance field and above it are shown in Fig. 9. The evolution of parallel edge modes can be observed. Just before and after the ferromagnetic resonance (at 205 and 216 mT fields, respectively), spin magnetic moment fluctuation amplitude is uniform throughout the whole area of a disk except for the parallel edges. At the additional absorption features observed after the FMR at 232 and 256 mT fields, respectively, fluctuation amplitude becomes larger at the edges while throughout the rest of a disk, it goes to zero, in other words, the rest of the spins "freeze in."

APPENDIX C: MAGNETIZATION MAPS OF EDGE MODES IN AN ARRAY

In this Appendix we discuss the uniform precession and edge modes observed in the calculated FMR spectra in Fig. 4(a). At the resonance field, indicated by an arrow at 216 mT field in Fig. 4(a), the log FFT magnetization amplitude of spin magnetic moments is highest at the *perpendicular edge* area as in the single disk case but with the constrained magnetic moment area reduced (compare Fig. 9 amplitude maps of modes at 205 and 216 mT fields with a top panel in Fig. 10). When the external magnetic fields are approximately

229 and 250 mT, the *parallel edge modes* are excited. Mode maps reveal that in this case the magnetic moments fluctuate the most at the edges along disk coupling direction Fig. 10. This hints that disk interaction occurs through the fluctuating magnetic moments. As a result, along [10] direction the system becomes less stiff and resonance occurs at lower fields when the field is applied along [10] than along [11] direction as can be seen in the absorption spectra in Fig. 4(a) at around 229 and 251 mT fields.

In the real arrays such modes are absent due to shape imperfections and edge roughness of the disks arising from a lithographic fabrication method. Furthermore, due to computational limitations, we calculated significantly smaller amount of nanodisks than the real sample actually contains [22]. This is also further supported by micromagnetic simulations performed accounting for shape and edge imperfections which do not reproduce these modes [21].

[1] M. Krawczyk and D. Grundler, J. Phys.: Condens. Matter **26**, 123202 (2014).

[2] C. Nisoli, V. Kapaklis, and P. Schiffer, Nat. Phys. **13**, 200 (2017).

[3] V. S. Bhat and D. Grundler, Phys. Rev. B **98**, 174408 (2018).

[4] M. B. Jungfleisch, W. Zhang, E. Iacocca, J. Sklenar, J. Ding, W. Jiang, S. Zhang, J. E. Pearson, V. Novosad, J. B. Ketterson, O. Heinonen, and A. Hoffmann, Phys. Rev. B **93**, 100401(R) (2016).

[5] T. Shinjo, T. Okuno, R. Hassdorf, K. Shigeto, and T. Ono, Science **289**, 930 (2000).

[6] R. P. Cowburn, D. K. Koltsov, A. O. Adeyeye, M. E. Welland, and D. M. Tricker, Phys. Rev. Lett. **83**, 1042 (1999).

[7] V. Castel, J. Ben Youssef, F. Boust, R. Weil, B. Pigeau, G. de Loubens, V. V. Naletov, O. Klein, and N. Vukadinovic, Phys. Rev. B **85**, 184419 (2012).

[8] O. Heinonen, Phys. Rev. B **92**, 054420 (2015).

[9] J. Ding, P. Lapa, S. Jain, T. Khaire, S. Lendinez, W. Zhang, M. B. Jungfleisch, C. M. Posada, V. G. Yefremenko, J. E. Pearson, A. Hoffman, and V. Novosad, Sci. Rep. **6**, 25196 (2016).

[10] E. Östman, U. B. Arnalds, E. Melander, V. Kapaklis, G. K. Pálsson, A. Y. Saw, M. A. Verschuuren, F. Kronast, E. T. Papaioannou, C. S. Fadley, and B. Hjörvarsson, New J. Phys. **16**, 053002 (2014).

[11] R. Dutra, D. E. Gonzalez-Chavez, T. L. Marcondes, R. L. Sommer, S. O. Parreiras, and M. D. Martins, Phys. Rev. B **99**, 014413 (2019).

[12] M. Demand, A. Encinas-Oropesa, S. Kenane, U. Ebels, I. Huynen, and L. Piraux, J. Magn. Magn. Mater. **249**, 228 (2002), International Workshop on Magnetic Wires.

[13] N. Kuhlmann, A. Vogel, and G. Meier, Phys. Rev. B **85**, 014410 (2012).

[14] J. Sklenar, V. S. Bhat, L. E. DeLong, O. Heinonen, and J. B. Ketterson, Appl. Phys. Lett. **102**, 152412 (2013).

[15] J. Sklenar, P. Tucciarone, R. J. Lee, D. Tice, R. P. H. Chang, S. J. Lee, I. P. Nevirkovets, O. Heinonen, and J. B. Ketterson, Phys. Rev. B **91**, 134424 (2015).

[16] O. N. Martyanov, V. F. Yudanov, R. N. Lee, S. A. Nepijko, H. J. Elmers, R. Hertel, C. M. Schneider, and G. Schönhense, Phys. Rev. B **75**, 174429 (2007).

[17] M. Hänze, C. F. Adolff, B. Schulte, J. Möller, M. Weigand, and G. Meier, Sci. Rep. **6**, 22402 (2016).

[18] Y. Wei, R. Brucas, K. Gunnarsson, I. Harward, Z. Celinski, and P. Svedlindh, J. Phys. D **46**, 495002 (2013).

[19] A. Vansteenkiste, J. Leliaert, M. Dvornik, M. Helsen, F. Garcia-Sanchez, and B. Van Waeyenberge, AIP Adv. **4**, 107133 (2014).

[20] M. Mulazzi, A. Chainani, Y. Takata, Y. Tanaka, Y. Nishino, K. Tamasaku, T. Ishikawa, T. Takeuchi, Y. Ishida, Y. Senba, H. Ohashi, and S. Shin, Phys. Rev. B **77**, 224425 (2008).

[21] A. Ciuciulkaite, Master's thesis, Department of Physics and Astronomy, Uppsala University, 2016.

[22] M. B. Jungfleisch, J. Sklenar, J. Ding, J. Park, J. E. Pearson, V. Novosad, P. Schiffer, and A. Hoffmann, Phys. Rev. Appl. **8**, 064026 (2017).

[23] A. Farhan, P. M. Derlet, A. Kleibert, A. Balan, R. V. Chopdekar, M. Wyss, L. Anghinolfi, F. Nolting, and L. J. Heyderman, Nat. Phys. **9**, 375 (2013).

[24] V. Kapaklis, U. B. Arnalds, A. Farhan, R. V. Chopdekar, A. Balan, A. Scholl, L. J. Heyderman, and B. Hjörvarsson, Nat. Nanotech. **9**, 514 (2014).

[25] M. S. Andersson, S. D. Pappas, H. Stopfel, E. Östman, A. Stein, P. Nordblad, R. Mathieu, B. Hjörvarsson, and V. Kapaklis, Sci. Rep. **6**, 37097 (2016).

[26] S. Gliga, A. Kákay, R. Hertel, and O. G. Heinonen, Phys. Rev. Lett. **110**, 117205 (2013).

[27] E. Iacocca, S. Gliga, R. L. Stamps, and O. Heinonen, Phys. Rev. B **93**, 134420 (2016).

[28] X. Zhou, G.-L. Chua, N. Singh, and A. O. Adeyeye, Adv. Funct. Mater. **26**, 1437 (2016).

[29] E. Östman, H. Stopfel, I.-A. Chioar, U. B. Arnalds, A. Stein, V. Kapaklis, and B. Hjörvarsson, Nat. Phys. **14**, 375 (2018).

[30] M. Kammerer, M. Weigand, M. Curcic, M. Noske, M. Sproll, A. Vansteenkiste, B. Van Waeyenberge, H. Stoll, G. Woltersdorf, C. H. Back, and G. Schütz, Nat. Commun. **2**, 279 (2011).